Lakshminath Kundanati: Nanoindentation experiments on mandible, MicroCT experiments, Mandible SEM, Cutting mechanical model, Writing. **Nimesh R. Chahare:** 3D model of mandible, Finite Element simulations, Wood indentation experiments. **Siddhartha Jaddivada:** Finite Element simulations with multiple boundary conditions, Digitization of videos. **Abhijith G. Karkisaval:** 3D model of mandible. **Rajeev Sridhar:** Compression and density properties of wood. **Nicola M. Pugno:** Cutting mechanical model conceptualization, development, supervision, data analysis, funding acquisition, writing, reviewing, and editing. **Namrata Gundiah:** Project Conceptualization, Supervision, SEM of wood samples, Data Analysis, Funding Acquisition, Writing, Reviewing and Editing.

Cutting mechanics of wood by beetle larval mandibles

Lakshminath Kundanati[1], Nimesh R. Chahare[2], Siddhartha Jaddivada[2], Abhijith G. Karkisaval[2], Rajeev Sridhar[2], Nicola M. Pugno[1,3,4] and Namrata Gundiah[2]*

[1]Laboratory of Bio-inspired, Bionic, Nano, Meta Materials and Mechanics, Department of Civil, Environmental and Mechanical Engineering, University of Trento, via Mesiano 77, I-38123 Trento, Italy.

[2]Department of Mechanical Engineering, Indian Institute of Science, Bangalore.

[3]School of Engineering and Materials Science, Queen Mary University of London, Mile End Road, E1 4NS London, United Kingdom.

[3]Ket-Lab, Edoardo Amaldi Foundation, Via del Politecnico snc, I-00133 Roma, Italy.

*Correspondence to: Namrata Gundiah, Biomechanics Laboratory, Mechanical Engineering department, Indian Institute of Science, Bangalore 560012, INDIA.

Email: namrata@iisc.ac.in ; ngundiah@gmail.com

Telephone (Off/Lab): +91 80 2293 2860/ 3366

Abstract

Wood boring is a feature of several insect species and is a major cause of severe and irreparable damage to trees. Adult females typically deposit their eggs on the stem surface under bark scales. The emerging hatchlings live within wood during their larval phase, avoiding possible predation, whilst continually boring and tunneling through wood until pupation. A study of wood boring by insects offers unique insights into the bioengineering principles that drive evolutionary adaptations. We show that larval mandibles of the coffee wood stem borer beetle (*Xylotrechus quadripes:* Cerambycidae*)* have a highly sharp cusp edge to initiate fractures in *Arabica* wood and a suitable shape to generate small wood chips that are suitable for digestion. Cuticle hardness at the tip is significantly enhanced through zinc-enrichment. Finite element model of the mandible-showed highest stresses in the tip region; these decreased to significantly lower values at the start of the hollow section. A hollow architecture significantly reduces bending stresses at mandibular base without compromising the structural integrity. A scaling model based on a fracture mechanics framework shows the importance of the mandible shape in generating optimal chip sizes. These findings contain general principles in tool design and put in focus interactions of insects and their woody hosts.

1. Introduction

Wood boring (xylophagous) beetles cause irreversible damage to forests, crops, and timber due to their impact on transport of sap and nutrients in stems [1, 2]. The larval ability to tunnel inside wood allows them to successfully evade their natural enemies when accessing a nutritional source for which there is reduced competition. The remarkable success of xylophagous insects mainly lies in the larval ability to repeatedly cut through hard substrates over a long duration. Although these insects are among the leading threats to forests and tree plantations across the world, little is known about the mechanics of their mandibles in wood boring. Mandibular design requires a structure that can be repeatedly used to easily cut through wood fibers without itself undergoing fracture, wear or failure. Another essential requirement is the generation of small wood chips which may easily be ingested by the insect. Of equal importance is the toughness of the mandibular cuticle and its ability to withstand the structural stresses during boring. A combination of toughness and hardness facilitates diverse functions in beetle mandibles such as cutting, digging, combat, etc [3, 4].

The cuticle of insect mandibles is mainly composed of proteins, lipids, and carbohydrates (in the form chitin), which are hierarchically organized into stratified layers to produce one of the toughest known natural composites [4, 5]. Mechanical properties of the cuticle can range from being hard in many larval or adult mouthparts to highly flexible in the intersegmental membranes; such adaptations permit a diverse functional repertoire of the cuticle in insects [6, 7]. The vast range of mechanical properties of the cuticle is dictated by sharp variations in its material composition through incorporation of transition metals and halogens [4, 8, 9], or through *sclerotization* in which the cuticular proteins are stabilized through a variable degree of quinone reactions [10, 11]. Unlike the hard enamel coatings of mammalian teeth, hardness in

insect mandibles is enhanced through metal-ion mediated crosslinking of chitin-protein complex molecules [12]. Such hardening mechanisms have been reported in diverse insect mandibles of termites, leaf cutter ants, and jaws of a nereid worm, *Nereis virens,* etc. through the incorporation of transition metals like zinc and manganese [13–17]. To investigate the mechanisms of wood boring in insects, we studied the coffee white stem borer (CWSB), *Xylotrechus quadripes*, which bores through coffee stems (*Coffea Arabica* L.*)* during an 8-10 month long developmental period [18]. The beetle larvae chew through the stem, thereby severely reducing the production of coffee beans, and ultimately cause the destruction of entire plantations [2].

The goals of our study are to characterize the structure-property relationships of the CWSB larval mandibles and analyze its response to the mechanical stresses encountered during wood chipping. First, we characterize the surface morphology and the compositional variation at different locations in the mandible using scanning electron microscopy with X-ray microanalysis. We also quantify the three-dimensional structure of the mandible using microtomography. Second, we estimate the mechanical properties of the mandibles at different locations using nanoindentation and correlate these with the compositional analysis. Third, we quantify the material properties of the wood substrate and compare these with that of the larval mandibles. Finally, we use a scaling model of two indenters cutting through a quasi-brittle wood material to characterize the relationship between the mandible shape and the chip sizes generated during cutting. The study explores biomechanical design principles and puts into focus the interactions of insects and their wood-hosts, and may provide novel guidelines for engineers who design boring and cutting tools.

2. Materials and Methods

2.1. Mandibles of Coffee Wood Stem Borers

Fourth and fifth stage larvae of coffee white stem borer (*Xylotrechus quadripes* Chevrolat; Coleoptera, Cerambycidae; CWSB) were collected from uprooted infested coffee stems (*Coffea arabica* L.*)* from plantations in the Western Ghats in Karnataka, India, stored in 100% ethanol, and transported to the laboratory. Mandible specimens were dissected from the larvae, cleaned using ultrasonication, and prepared for the experiments (Fig. 1B). Once dissected, the mandibles of CWSB larvae were cleared of the muscles and other soft tissues, and imaged using bright-field microscopy. Specimens were embedded in acrylic resin and polished to achieve a flat surface for nanoindentation and compositional analysis.
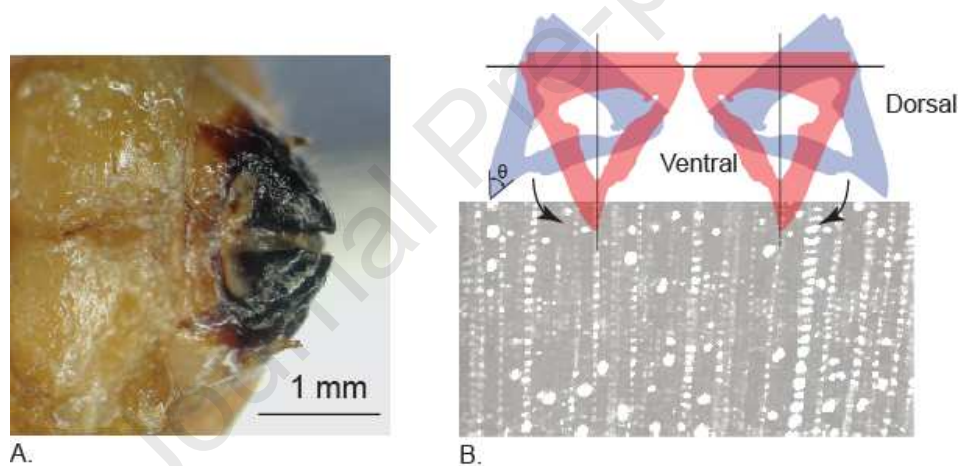

Figure. 1A: Larvae mandibles show darkened and sclerotized cutting regions. **B:** Schematic of a representative tangential section of the anisotropic wood substrate during mandible movement. The distance of the mandible axis from the tip is approximately 0.5 mm which is approximately the mandible height. Image of the wood microstructure is adapted from [19].

Video observations show a larva rotating its head when cutting through an uprooted and sectioned coffee stem (Movie S1). A schematic of the mandible movement during wood cutting is shown in Figure 1B. The optical images of coffee wood section in the figure are adapted from

[19] to presents a possible scenario for mandible movements in the tangential direction in the anisotropic wood substrate (Figure 1B).

2.2. *Scanning Electron Microscopy (SEM) and Energy Dispersive X-ray Spectroscopy (EDX)*

The prepared mandibles were carefully mounted on double-sided carbon tape (Electron Microscopy Sciences, USA), attached to an aluminum stub, and placed in a desiccator to avoid contamination. Specimens were transferred to a sputter coater (Bal-Tec SCD 500, Liechtenstein), the chamber purged thrice with argon, and the mandibles coated with a thin gold layer. A scanning electron microscope (Quanta 200 ESEM, FEI, The Netherlands) was used to image the samples with accelerating voltages between 5 and 20 kV. To quantify the elemental composition of mandibles, polished specimens were mounted on carbon tape and coated with a 10 nm layer of gold. EDX detector in the SEM was used to scan the samples and the spectra collected using an accelerating voltage of 20 kV. A custom software (Genesis, FEI) was used to identify the individual peaks in a given spectrum. Variations in zinc along the length of the mandible were determined using a line scan. A pure zinc sample was used as reference for the calibration of these spectra.

2.3. *X-Ray microtomography of the mandibles*

We used a non-destructive X-ray microtomography (microCT) technique to obtain three - dimensional images of the mandible and its connecting musculature. To prepare the samples for microCT, the larval head containing the mandible was cleaned with ethanol to remove possible debris, and the labrum and clypeus were mechanically dissected from the body. The specimen was fixed in Bouin's solution for 16 hours, dehydrated using graded solutions of ethanol (30% - 100%; 10 minutes each), and stained using iodine (1g in 10 ml of 100% ethanol) for 24 hours to

improve the optical contrast between the cuticle and soft tissues [20]. A toothpick was used to mount the air-dried sample on the specimen holder in the microCT instrument (Xradia Versa XRM 500). A beam of X-rays of 60 kV accelerating voltage (6W) was incident on the sample and the projected plane was recorded to obtain a two - dimensional image. A set of 2500 projections was obtained by rotating the sample at small discrete angles about the vertical axis and a 3D structure was reconstructed using XRM software. A raw threshold was used to reduce the background noise for better visualization in the images. The reconstructed dataset was analyzed using AMIRA (v6.0.1, XEI Software, The Netherlands) to extract structural details including the connecting musculature and volume of the hollow regions within the mandible.

2.4. *Density and uniaxial compression of wood samples*

We used a uniaxial testing machine (Mecmesin Multitest 10-i, UK), equipped with a 10 kN load cell, to quantify the monotonic compression results from wood specimens in the longitudinal direction (*Coffea arabica* L.*)*. Specimens were prepared according to Indian Standard for wood testing (IS:1708) by machining sections in the parallel (2 cm $\times$ 2 cm $\times$ 8 cm; n=8) Samples were soaked in water for 45 hours to reach fiber saturation point (FSP), the specimen thickness measured using calipers, and the samples were mounted using compression platens in the testing frame. The sample was preloaded to 500 N and tested under compression (1 mm/sec) to characterize the material properties. Forces recorded using a load transducer, were converted to engineering stresses using initial specimen dimensions, and the strains were calculated by measuring encoder displacements during specimen loading. Young's modulus was calculated using the initial linear region of the stress-strain curve.

The density of wood samples (n=4) was determined by immersing samples in water and measuring the specimen volume using image processing. The dry mass of the sample was

7

obtained by drying the sample in an oven at 100°C. Specimen masses after equilibration, corresponding to FSP and dry conditions, were used in the calculation of the wood density [21].

2.5. *Microindentation of wood samples*

The wood samples were cut in the plantation, transported to the lab located about 200 km from plantation on the same day, stored in cool conditions and tested within 4 days after cutting We used microindentation experiments to quantify the hardness in the transverse plane of Arabica wood samples. Specimens were polished using a series of 400, 800, 1200, 2000 and 4000 grade sandpaper, cleaned for a debris free surface, and indented in a CSM micro indenter using a standard Vickers tip with a maximum of 10 N load and at a loading rate of 5 N/min.

2.6. *Nanoindentation of the mandible*

Ultrasonicated and cleaned CWSB mandibles, mounted in acrylic resin, were polished using sandpaper with varying grit sizes (200, 400, 600, 800, 1000, 1200, 1500, 2000) and diamond paste to achieve flat surfaces for mechanical studies. We used nanoindentation experiments on the prepared specimens using a 3-sided pyramidal Berkovich indenter (tip radius = 150 nm) to characterize the local mechanical properties. The specimen was loaded at 50 μNs^{-1} up to a maximum load of 500 μN using a nanoindenter (TI 900-Tribo Indentor, Hysitron, Minneapolis, MN, USA). To reduce any possible effects of creep during unloading, we used a trapezoidal cycle consisting of 10 second loading, 5 second hold, followed by a 10 second unload period [22]. The resulting load-displacement data corresponding to the unloading curve were analyzed using custom software to determine the contact stiffness (S), reduced modulus (E_R), and hardness (H), defined as a ratio of the peak load to the projected area of contact of the tip with the indenter, based on the well-established Oliver and Pharr method [23].

A total of nine mandibles were tested with 8 indentations at regions varying from the tip to the mandibular base (Fig. 2C) These are labelled as the tip, intermediate, and base regions of the mandible. The intermediate region was located before the start of the hollow region within the mandible. Statistical analyses to test for differences in the different regions were performed using ANOVA with Bonferroni comparison using *multcompare* function in MATLAB. A p value of <0.05 was considered statistically significant.

2.7. *Finite Element simulations of the mandible*

Individual microCT images were used to obtain a three - dimensional model of the mandible. A surface reconstruction of the mandible boundary from each transverse section was obtained by segmenting the image using MATLAB R2014b (Version 8.4) (MathWorks, Natick, MA, USA). Ten different transverse bounding sections, taken with a gap of ~10 μm towards the mandible tip as compared to the base (~ 50 μm), were included in the construction of the 3D model. The coordinates of the bounding curves were imported as B-splines by including additional points between the coordinates on each bounding surface. Adjacent curves were next connected and shaped into a solid body using a loft feature (SolidWorks 2013, Concord, MA, USA) to obtain a three-dimensional model (Fig. 2A-B).

The model was meshed using 10-node tetrahedral elements (Hypermesh 9, Altair Hyperworks, Troy, MI, USA). A total of 16328 elements were initially generated to create a coarse mesh (length 20 μm) of the structure. We used the numerical finite element method (FE) to simulate a quasi-static condition of the mandible tip in contact with the substrate and loaded to simulate wood cutting. The structure was meshed (Fig. 2C) and uniformly assigned with Young's modulus value of 6 GPa in the tip region located ~15 μm from the mandible apex, intermediate region, and the base region of the mandible using averaged and rounded off values

from the nanoindentation studies. We assumed the value of ν as 0.3 [24]. Each of the two

mandibles move due to the action of adductor and abductor muscles that are located at the

mandible base (Movie S1; Movie S2). The pivot axis for mandible rotation was assumed to be

along the axis M-M' which was obtained from the videography of the borer (Fig. 2D; Movie S1).

Specifically, the individual mandible edges during movement were tracked and the lever axis

was determined to be located near the abductor muscles. The presence of a pivot axis, located

towards the abductor muscle attachment region, has also been reported in other model systems

such as the larvae of weevils, wood-boring ants, and dragonflies [25,26]. Points of attachment of

the abductor and adductor muscles to the mandibular base were determined using image

segmentation from X-ray microtomography (Movie S2). Three different boundary conditions

were used to assess stress distributions on the mandible; first, a pivot case was simulated using

M-M' as the lever axis. In this method, the movement of nodes in the mandible base, located in

proximity to M-M' axis, were constrained using rigid links to achieve the desired pivot motion.

Uniform tractions of 10 MPa were applied at surface S1 to simulate the action of adductor

muscle. Surface tractions of 35 MPa, based on published reports of rupture stress of Balsam

wood, were applied to elements located at the mandible tip ($\sim$15 µm) in a direction normal to the

surface in contact with the substrate [27]. Second, a semi pinned boundary condition in which

nodes were fixed only at adductor (S1 surface) and abductor muscle (S2 surface) attachments

located at the base region of the mandible (Fig. 2E). Finally, a fully pinned case where nodes

corresponding to the mandible base had zero translational displacements (Fig. 2F). Mechanical

equilibrium equations for the discretized structure were solved at each node using the prescribed

boundary conditions using a commercial solver (Abaqus 6.11, Dassault Systèmes, Providence,

RI, USA). Displacement and stress distributions were quantified in various regions of the

mandible; solution convergence was assessed by mesh refinement to within 5% error between consecutive meshes. The final mesh used in reporting the solutions had 134707 elements which had varying lengths from the tip to the mandible base.
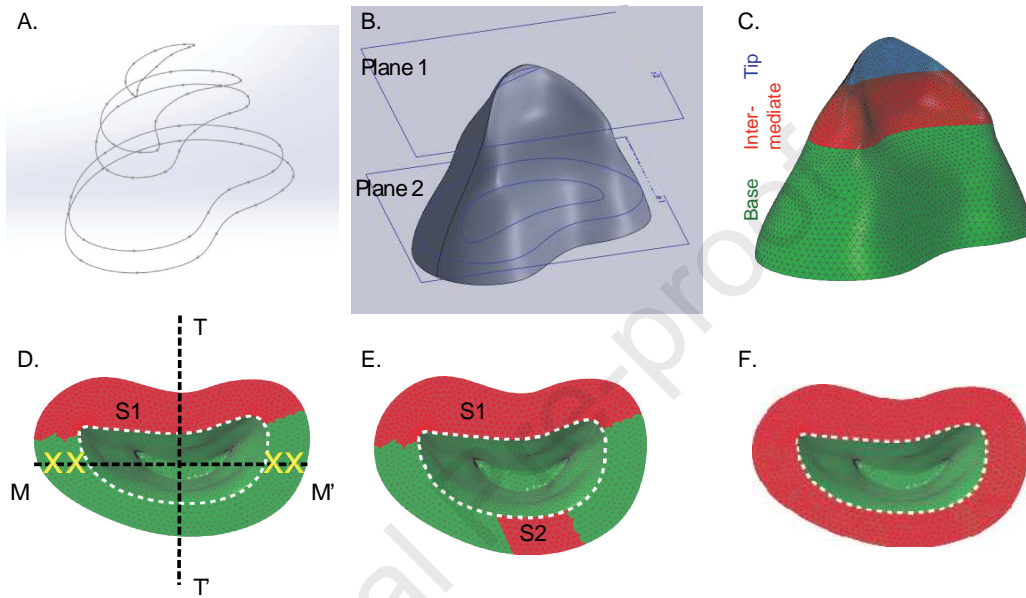

Figure. 2A: Splines were constructed using the microCT results at different heights from the base to the tip of the mandible that were used for constructing a 3D geometrical model **B:** The model after reconstruction is shown with cross-sectional planes in the tip region corresponding to plane 1 (solid) and a hollow region (plane 2). **C:** The structure was meshed and divided into the tip (blue), intermediate (red), and base (green) regions of the mandible. **D:** Surfaces S1, located at the base of the mandible, corresponded to the attachments of the adductor muscle. This, along with the axis of rotation (M-M'), and the rigid links represented with yellow crosses, were used to impose the pivot boundary conditions to compare stress distributions on the mandible. T-T' refers to the sagittal plane through the mandible. **E:** A semi pinned boundary condition shows fixed nodes at adductor (S1 surface) and abductor muscle (S2 surface) attachments at the base

region of the mandible. **F**: All nodes at the mandible base (in red) had zero translational displacements for the fully pinned boundary condition.

2.8. *Scaling model of the mandibles in generating wood chips*

We developed a simple scaling model of the two mandibles indenting the wood substrate. We model the two mandibles as two independent indenters that penetrate and generate cracks in the wood substrate. These cracks eventually meet to form a wood chip that may be ingested by the insect (Fig. 3).
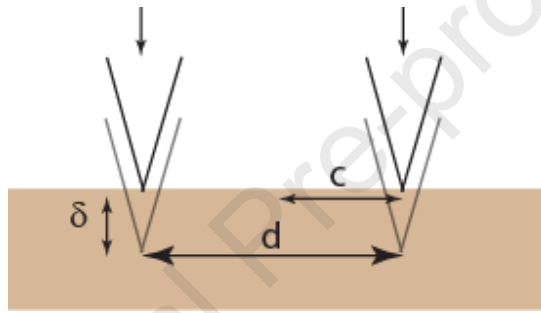

Fig. 3: Schematic of the mandibles modeled as two independent indenters penetrating the wood substrate.

Fracture toughness, K_{IC}, of the substrate during indentation is expressed in terms of the Young's modulus, E, substrate hardness, H and the load for crack formation, P_{max}, using the Lawn-Evans-Marshall (LEM) model given by [28,29]:

$$K_{IC} = \alpha \left(\frac{E}{H}\right)^{0.5} \left(\frac{P_{max}}{c^{3/2}}\right) \tag{1}$$

Where c is the length of the longest crack taken from the center of the indenter, and α is a dimensionless constant. For example, α=0.016 for Vickers indenter interacting with brittle materials. LEM coefficient (α) was derived empirically and theoretically in earlier studies and depends on the material type and indenter geometry [30,31].

We use a modified LEM coefficient with a generalized fracture mechanics approach to incorporate the discrete nature and plasticity of the wood substrate [32,33] :

$$\alpha' = \frac{\alpha}{\left(1+\frac{c_o}{c}\right)^{2-\frac{\eta}{2}}}, \quad \eta = \frac{\kappa}{\kappa+1} \tag{2}$$

where, c_o is the average wood cell size, and η the strain hardening coefficient. The exponent of constitutive power law $(\kappa) = 1$ indicates elastic response, $\kappa < 1$ denotes elastic plasticity, and $\kappa > 1$ denotes hyperelasticity. The modified fracture toughness equation is:

$$K_{IC} = \frac{\alpha}{\left(1+\frac{c_o}{c}\right)^{2-\frac{\eta}{2}}} \left(\frac{E}{H}\right)^{0.5} \left(\frac{P_{max}}{c^{3/2}}\right) \tag{3}$$

The maximum size chip formation occurs under an optimal condition given by:

$$d = 2c \tag{4}$$

Where d is the separation distance between the indenters (Fig. 3A). The applied load (P) is related to the penetration depth of indenter (δ) as

$$P_{max} = HA \tag{5}$$

A is the projection of the contact area due to indentation and β is a constant which is dependent on the tip geometry. We consider an axisymmetric profile for the mandible, represented as an indenter, and given by a power law with exponent γ:

$$\frac{h}{h_o} = \left(\frac{r}{r_o}\right)^{\gamma} \tag{6}$$

where, r is the radius and h is the height at a given location, and r_0, h_0 are base radius and height respectively. Using equation (6), we write the projected area of contact A during indentation as:

$$A = \pi \left(\frac{h}{h_o}\right)^{2/\gamma} r_o^2 \tag{7}$$

and inserting equations 4, 5, and 7 in equation 3, we write a general scaling law which describes the optimal chipping with inclusion of plastic and porous nature of wood, as

$$\left(\frac{\delta}{h_o}\right)^{\frac{2}{\gamma}}(\pi r_o^2) = \left(\left(\frac{(d+2c_o)^{\left(2-\frac{\eta}{2}\right)}}{d^{\left(\frac{1-\eta}{2}\right)}}\right)\frac{K_{IC}}{\alpha\sqrt{8HE}}\right);\begin{cases}\delta = \delta_{el-pl}\ ;\ \kappa < 1\\\delta = \delta_{el}\ ;\ \kappa = 1\\\delta = \delta_{hy-el}\ ;\ \kappa > 1\end{cases} \qquad (8)$$

where, $\delta_{el-pl},\ \delta_{el},\ \delta_{hy-el}$, correspond to the elastic-plastic, elastic and hyper-elastic conditions. This equation also suggests that the animal may modulate the penetration depth of the indenter to achieve optimal chip formation for a given substrate. The wedge angle (θ) of the tip represents the vertex angle of the mandible was measured using the scanning electron micrographs of the mandible cross-section (Fig.1B).

3. Results and Discussion

3.1. *Mandible morphology and zinc enrichment in the tip regions*

The mandibles were visibly darker than the larval body (Fig. 1A). Scanning electron microscopy (SEM) characterization of the mandible morphology revealed a curved and sharp edge located towards the tip of the cutting regions with a relatively thicker base (Fig. 4A, B). The radius of curvature of the cutting edge, as measured in the cross-section of the polished mandible, was less than 0.5 µm (Fig. 4C); this is also characteristic of tools such as scalpel blades which typically have 0.25 µm. Energy dispersive X-ray spectroscopy detector (EDX) in the SEM, was used to characterize the presence of elemental transition metals, including zinc, at different spatial locations in the mandible (Fig. 5A). Analyses of the mandible surface show a clear overlap of the peaks corresponding to zinc located preferentially in the tip region of the mandible but not in the base regions (Fig. 5B). Linear scans of the EDX spectra from cross-sections of the polished mandibles also show that the presence of zinc steeply increased in the tip region as compared to the base (Fig. 5C). The presence of zinc is hence exclusive to the cutting regions of the mandible tip whereas the neighboring regions are devoid of zinc. In an earlier study, we showed the importance of zinc in the ovipositor of fig wasp parasitoid insects (*Apocrypta* spp.) in increasing

14

the cuticular hardness to aid insects in cutting through hard substrates [9]. A higher material hardness of ant mandibles is also known to correlate with the presence of transition metals in the articulating surfaces [4]. We work on the hypothesis that zinc recruitment increases the hardness of the mandible tip as compared to base regions which do not come into contact with the wood substrate.
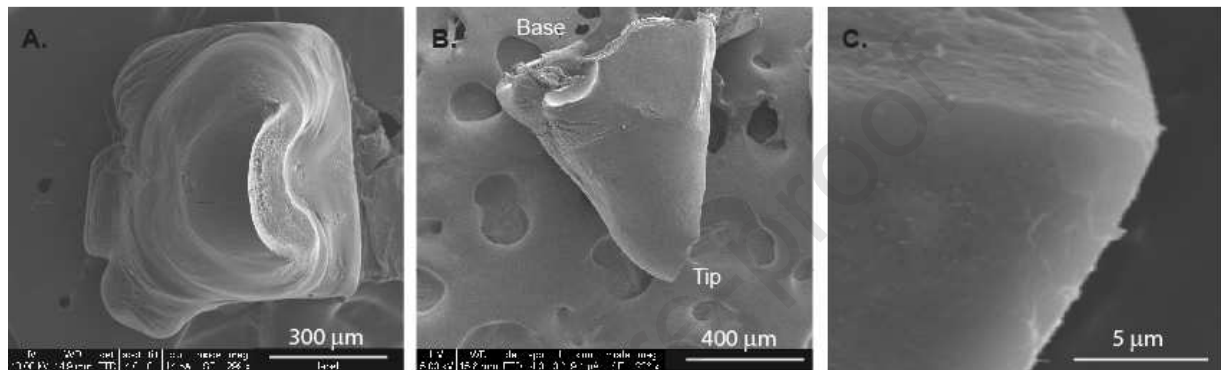

Figure. 4A: Scanning electron micrograph of the top of the CWSB mandible sample brings into focus the curved cutting parts of the tip region of the mandible. **B:** Side view highlights the surface of the mandible and the cutting cuspal edge. **C:** Zoomed view of the edge region of the mandible to demonstrate the tip sharpness which was measured to be 0.5 μm.

3.2. *Mechanical properties of the mandible and coffee wood*

The force-depth curves, obtained using nanoindentation with a Berkovich indenter, showed clear differences in the mechanical properties from the tip of the mandible region as compared to other regions (Fig. 5E). We analyzed the force-depth relationships based on the standard Oliver-Pharr method in nanoindentation, and tested for variance in mechanical data between the tip, intermediate, and base regions of the mandible. Our results showed that the contact stiffness in the intermediate (8.63±1.66 N/mm) and base (9.14±1.97 N/mm) regions of

the mandible were similar (Table A1) and significantly higher as compared to the tip region (7.13± 0.87 N/mm; p<0.05). In contrast, mandible hardness in the tip region (0.67± 0.20 GPa; p<0.05) was significantly greater than both the base (0.36±0.06 GPa) and the intermediate region (0.40±0.06 GPa). These results are in agreement with earlier studies on incorporation of transition metals such as zinc, manganese, copper, and iron in the cuticle that increase the local hardness and may improve material wear resistance [8,9]. The mandibles of termites (Cryptotermes primus) which feed on dry wood were observed to be more scratch resistant as compared to the sub-families without the zinc and this was attributed to the presence of zinc [35].

Broomell and co-workers demonstrated the role of transition metals (Zn, Cu, and Mn) in altering the hardness and stiffness of a model marine polychaete annelid jaw (*Nereis virens)* using differential chelation experiments [15,16]. These studies showed that the presence of transition metals, mediated through the crosslinking of histidine-rich proteins in the cuticle, resulted in a step-gradient in hardness. Such gradients in material properties along the mandible lead to redistribution in the stress distributions near the sharp contact and an improved ability in resisting crack propagation between two materially distinct regions through deflection [36]. The insect cuticle is a functionally graded composite material with hierarchical architecture. Finite element model of a spider fang, based on the differential organization of individual materials in combination with functional grading, demonstrate a structure which is adapted for damage resilience and effective structural stiffness [37]. Graded material properties may also prevent the propagation of fractures between two materially distinct regions. How do the material properties of the mandible compare with that of wood? We used monotonic compression and micro-indentation experiments to quantify the mechanical properties of *Arabica* wood in the transverse

direction. The compression modulus of *Arabica* was 1039.5 ± 194.5 MPa. For a given load, tips with a smaller radius and higher stiffness produce higher contact stresses in the Hertzian contact theory. When the applied force reaches a critical value, fractures initiate at a depth ~ r/2 below the contact surface and propagate with an increase in the force. A higher tip hardness as compared to the substrate hence helps resist damage due to contact stresses [38]. Hardness of wood samples was significantly lower (30.9 ± 5.3 MPa) as compared to that of the mandible tip (0.67± 0.20 GPa; p<0.01). Nanohardness for soft and hard woods at the fiber level is reported to be about ten times higher than the measured Brinell hardness [34]. Our results hence show that the mandible hardness is higher than the hardness at the wood fiber level.
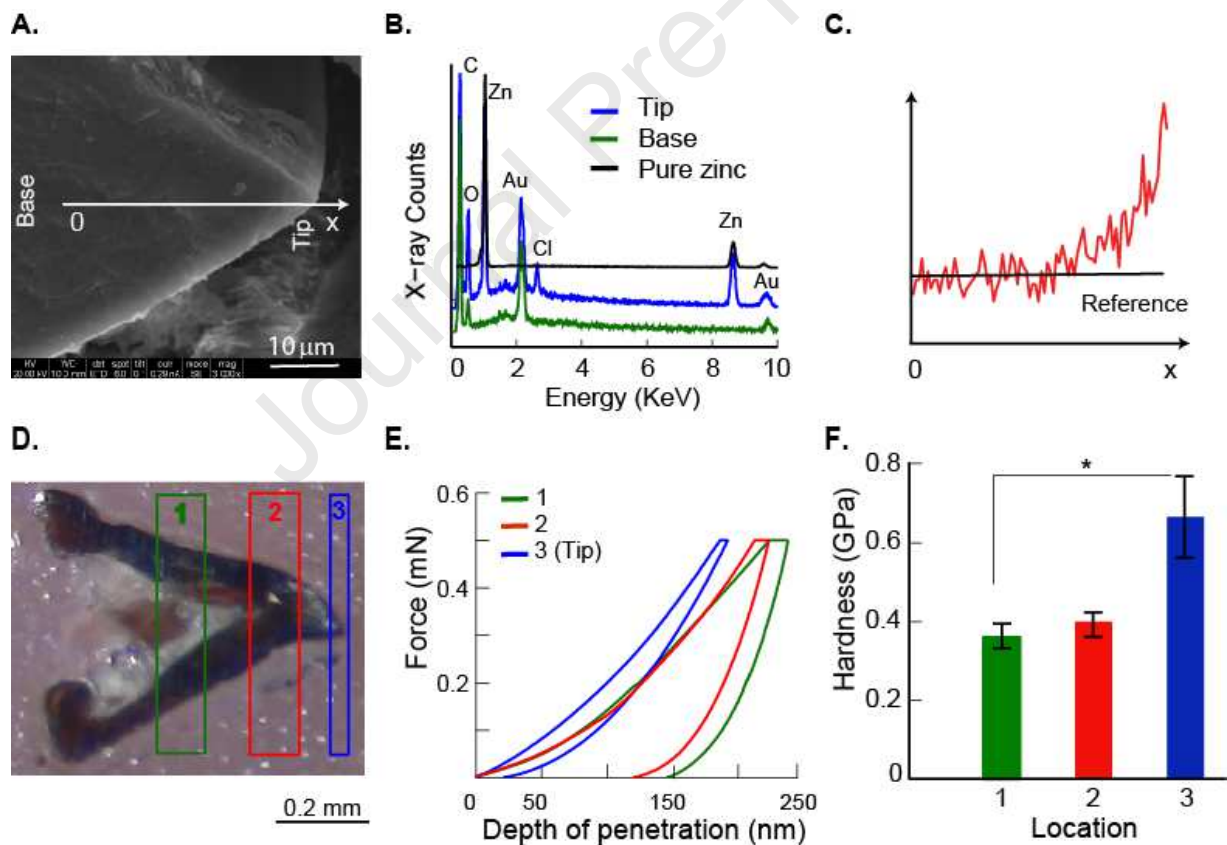

Figure. 5A: SEM image shows the base and tip regions of the mandible. **B**: Representative EDX spectra show peaks corresponding to zinc in the tip region alone as compared to the base.

Related peaks from gold, chlorine, carbon, and oxygen are also marked. **C**: Spectrum for a representative line scan from the base to tip in the specimen mandible shows an increase in zinc content towards the mandible tip region as compared to the base. **D:** Three regions were selected for nanoindentation studies on a polished mandible sample to quantify possible differences in regional material properties. **E**: Force–depth relationships show lower values of final depth from region 3 (tip) as compared to other regions shown in 5D. **F:** Bar plots from indentation experiments show significantly higher hardness ($p<0.05$), plotted as average $\pm$ standard deviation, for the tip as compared to the base region.

3.3. *Finite Element Analysis of the mandible during a simulated bite*

Are there any morphological adaptations in the mandible that make the larva effective in wood boring from a biomechanical perspective? X-ray microtomographic (XRadia Versa XRM 400) three-dimensional reconstruction of the mandible revealed a highly curved and sharp cutting edge with an internally localized conical hollow region which is clearly visible in the sagittal (Fig. 6A-B, Movie S2), coronal and transverse projections (Fig. 6C-D). Volume of the hollow region was approximately half the total mandible volume (53.0 ± 8.3 %, n=3; AMIRA 6.0.1, FEI software) which makes the mandible a relatively light structure (Movie S2).
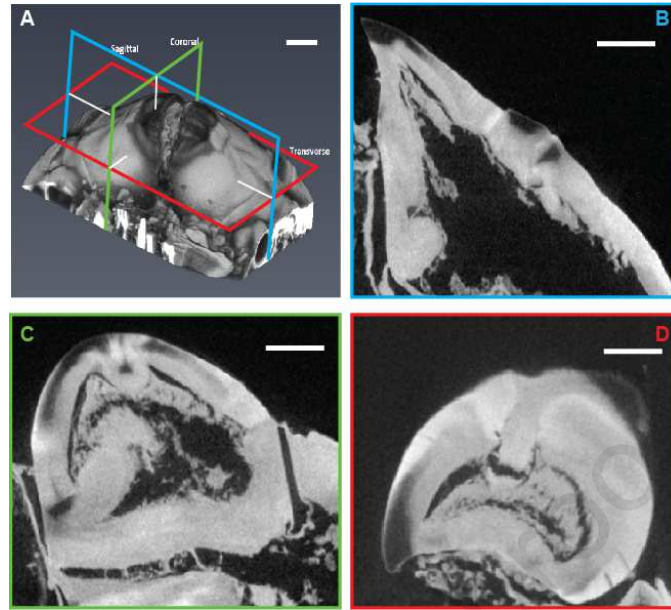
Figure. 6A: Three dimensional rendered microCT image of a borer mandible with highlighted sectional planes. **B**: Projection along sagittal plane shows a conical hollow part and a sharp cutting edge. **C**: Projections along coronal plane and **D**: transverse plane shows a curved mandibular region with a bean-shaped relatively hollow region.

We investigated the role of this hollow region in regard to the stress distributions on the mandible during substrate boring. We developed a finite element model as discussed in the Methods section and used uniform material properties, with a modulus of 6 MPa, from the nanoindentation studies on the discretized mandible structure (ABAQUS v6.12). Three different boundary conditions were applied which are referred to as fully pinned, semi pinned and pivot (Fig. 3 2D). The fully pinned condition allowed us to investigate the load-bearing capability of the mandible. The semi pinned case includes the effects of abductor and adductor attachments. Finally, the pivot case takes into account displacement of the mandible about the hinge axis (M-M') which is caused by the actuation of adductor muscle at the base of the mandible.

Figure 7 shows stress contours on various surfaces of the mandible for three different boundary conditions that correspond to the pivot, semi- pinned, and fully pinned cases (Fig. 2D-F) . Few differences are visible in the stress distributions at the tip of the mandible (region 3) which is primarily involved in cutting; maximum stress of ~ 155 MPa was present on the back surface. Stress differences among the different boundary conditions are apparent towards the muscle attachment points (region 1) and at the base surface of the mandible. The start of the hollow region within the mid-section of the mandible is highlighted using white boundary.
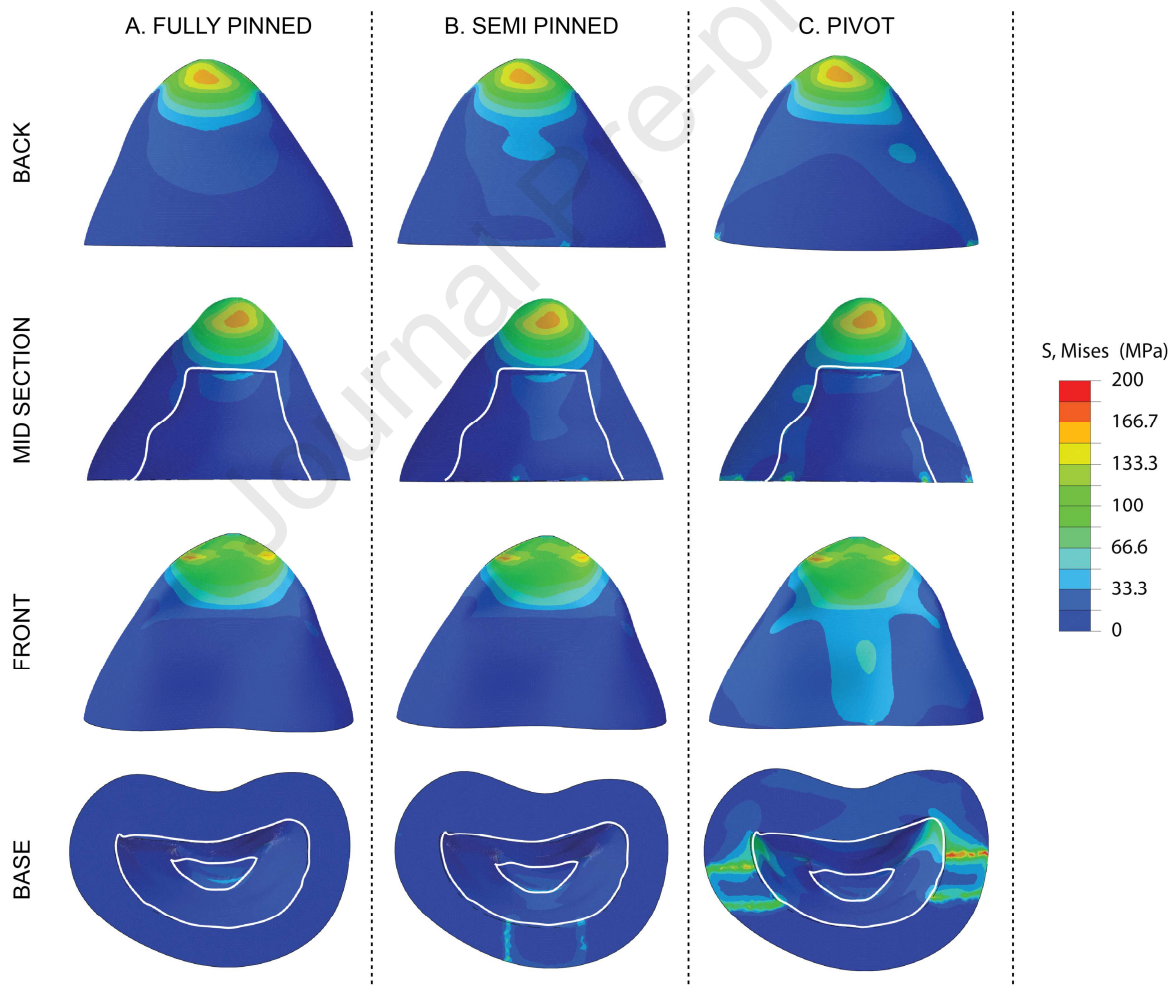
Figure 7: von Mises stress distributions corresponding to A) fully pinned, B) Semi pinned, and C) Pivot boundary conditions are shown on the back, midsection, front, and base surfaces of the mandible.

To explore for possible spatial variations, we plotted the von Mises stresses along the front and back outer bounding surfaces of the mandible on the sagittal section T-T' (Fig. 2D) along the length of the mandible in Figure 8. These results show that stresses had similar profiles for the fully pinned and semi pinned cases on the front and back surfaces of the mandible (Fig. 8). Stresses on the front surface of the mandible were ~ five times higher in Region 1 located towards the base of the mandible for the pivot case as compared to the two other cases. Stresses on the back surface decreased monotonically after a maximum traction in the region adjacent to the tip region; stress profiles were similar in the tip and intermediate regions for all three cases for the back surface (Fig. 8B).
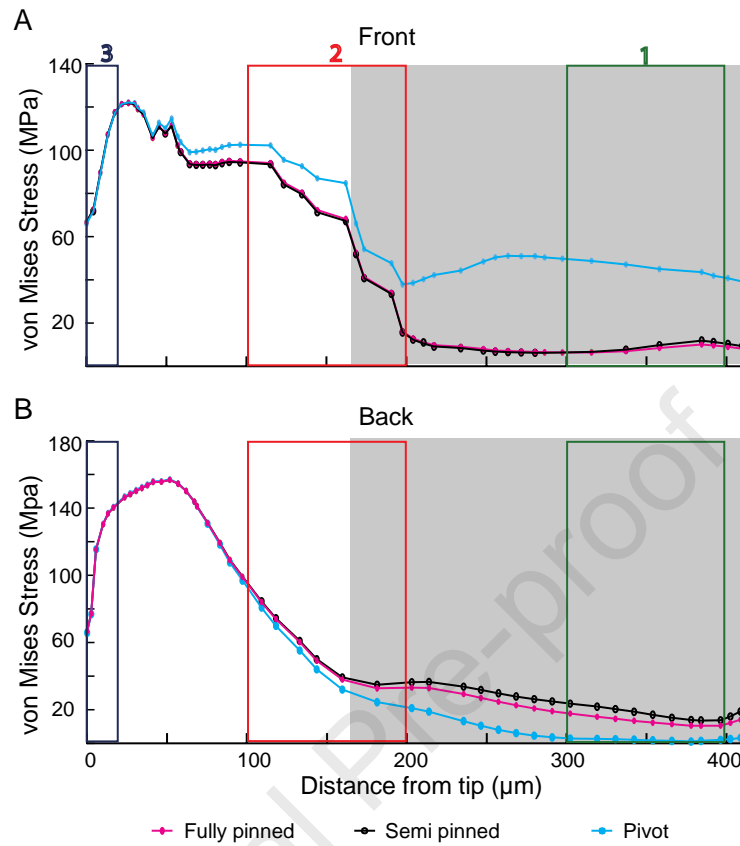
Figure 8: Comparison of stress distributions on the **A)** front and **B)** back surfaces of the mandible along the sagittal section (T-T') shown in Figure 2D. The distributions are plotted for the three different boundary conditions which were simulated in the study starting from the tip region. Regions where the material properties were quantified using nanoindentation are also included in the same figure using rectangular boxes.

Venom injecting structures in wasps and spiders experience acute stresses during their initial contact with the prey. Structural variations are hypothesized to reduce stress concentrations and prevent catastrophic failures in these structures during contact with the substrate [39]. The hollow structure in the mandible extended from ~165 microns at the tip to the base of mandible. This span coincides with regions on the back and front surfaces having less

stress (<90 MPa). The midsection surfaces in all the three simulations (Fig 7) show that in locations near the hollow region, marked by the white boundary, there is a sudden drop in stresses on both the front and back surfaces. Recent studies on ants which tunnel through wood showed the presence of short, cone-shaped mandibles with a wide articulatory base which rotate and help with concentrating muscle-generated forces to zinc-reinforced mandibular tips [25]. A similar rotator hinge mechanism with long mandibular output levers operate in male stag beetles to achieve forceful bites [26]. The presence of a hollow region also increases the toughness in absorbing the loads during impact loads. These biomechanical adaptations may hence aid in the cutting of wood by mandibles.

3.4.   Penetration into wood through mandibular action

Mechanical design of the mandibles hence reveals a combination of novel morphological and structural principles that make the beetle extremely effective in boring through wood. The low aspect ratio (~1.25) in mandible structures hence enhances their stiffness. Similar aspect ratios (1.45) are found in scorpion chela that also withstands high stress when feeding on hard shell preys [40]. The loading conditions in our simulations were idealized using solutions proposed for a cantilever beam of variable cross-sectional area [41]. Bending stress for a cantilevered structure, $\sigma_b = M/Z$, is low at the base where moment of inertia (I) and Z are large. In contrast, σ_b is high near the tip regions that experience uniform surface tractions during wood cutting (Fig. 7A-C). The mandible tip hence experiences higher tensile stresses on the ventral side (Fig. 2C). Hollow structures are also known to be stiffer than solid structures for a given material volume due to the greater moment of inertia and have lower material volume without compromising the function [5]. The mandible shape also determines the maximum size of the substrate chip which is an essential functional requirement in ingesting wood [42].

We developed a general scaling law to quantify the penetration of the mandible into wood using a fracture mechanics framework (Fig. 3). Wood is a quasi-brittle, anisotropic, and heterogeneous material with a hierarchical microstructure. Fracture toughness of wood depends on various factors including fiber orientation, mass density distribution, and submicroscopic features, such as cell wall structure, microfibril angle and the polymer assembly of the cells. External factors such as humidity, temperature or mode of loading also influence the measured mechanical properties of wood [43]. Water droplets in the wood cell lumen move away from the fracture process zone during loading [44] and the fluid pressure around the crack tip does not influence crack propagation resistance. Thus, the role of fluid in fresh wood crack propagation is negligible. Crack initiation in the radial, tangential and transverse directions is similar in five reported species of wood [45]. Because of the unavailability of fracture toughness values K_{IC} for Arabica wood, we used the corresponding values of Douglas fir, which has similar density and elastic modulus of the same order. The toughness values of Douglas fir are reported as 0.4 MPa·m$^{1/2}$ in mode I [46] and in the range of 0.4-0.61 MPa·m$^{1/2}$ in mode II [47]. The toughness of wood scales as (density)^2 for low-density woods and as (density)$^{1.5}$ for higher density woods [48]. We measured the density of *Arabica* wood to be 0.53 ± 0.004 g/cm^3 which is similar to a value of 0.51 g/cm^3 reported for Douglas fir [47]. Using the microCT data, we estimated the biting distance between mandibles to be between 0.1 mm and 0.5 mm. Equation (10) shows that the depth of cut is hence proportional to the distance between mandibles during biting. The vessel lumina in *Coffea arabica* were reported as < 50 µm, in diameter [19]. We hence assumed $c_o = 25$ µm in this study.

We used average measured mechanical properties of the coffee wood (transverse plane) measured from microindentation experiments (H=30.9 MPa and E=1.6 GPa) to calculate the

penetration depth during cutting of the wood substrate by the mandibles using the scaling model. We also explored variations in the indenter shape, γ, with the distance between indenters to estimate the values of δ using the model (Figure 9A-C). The values of δ are shown for variations in γ values and the plausible values were observed for γ <1 and conditions of elastic-plastic fracture (Table 1).

To consider the diversity of wood properties, we analytically estimated the depth of optimal cut (Table 1) for an order lower toughness (K_{IC}= 0.04 MPa $\sqrt{m}$) and higher toughness (K_{IC}= 4 MPa $\sqrt{m}$) values as that of the reference Douglas fir toughness, to include all other possible variations arising from the testing direction, humidity content and microstructure (Tables A2 and A3 show the range of estimated values). A small vertex angle may result in tool failure in tool design whereas a high vertex angle reduces the cutting ability of the tool [49]. By parametrically varying the vertex angles from 64° to 82° in turning processes showed that a wedge tool with 64° vertex angle was the most efficient for material removal [50]. The angle measurements from the cross-section of the mandible tip were in the range of ~47-52 ° when approximating it as a simple wedge.
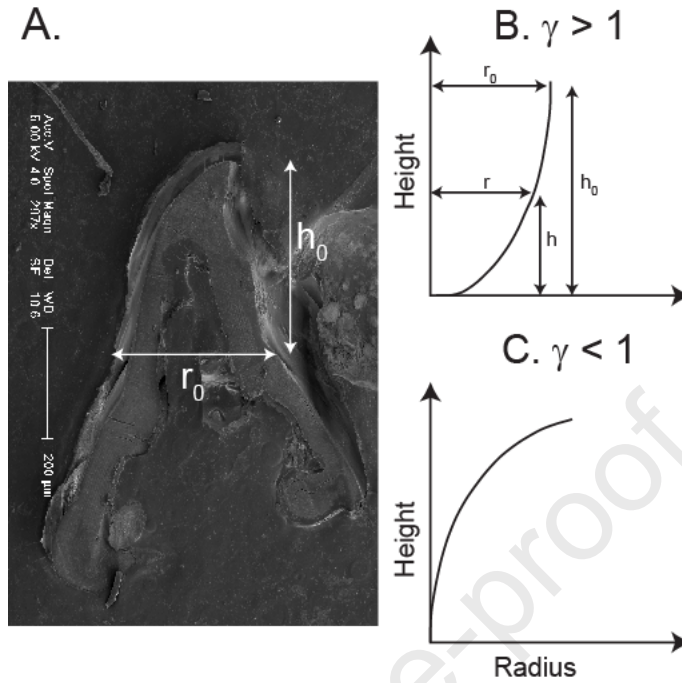
Figure 9A: SEM image of the mandible with representative diameter and height marked on the image. Schematic representations of the mandible model, assuming symmetric half edges, show variations in the radius (*r*) with height (*h*) for two cases with different shape factor values corresponding to **B:** $\gamma > 1$ and **C:** $\gamma < 1$. r_o, h_o are base radius and base height.

K_{IC} (MPa$\sqrt{m}$)	γ	δ_{el-pl} (μm)	δ_{el} (μm)	δ_{hy-el} (μm)	δ_{el-pl} (μm)	δ_{el} (μm)	δ_{hy-el} (μm)
		d = 100 μm			d = 500 μm		
0.04	0.1	397	395	393	435	435	435
	0.5	262	256	249	418	416	413
0.4	0.1	445	443	441	489	488	478
	0.5	466	454	443	744	740	735
4	0.1	499	497	494	539	538	538
	0.5	829	808	788	1214	1206	1199

Table 1: Depth of cut value, ($\delta_{el\text{-}pl}$, δ_{el}, δ_{el}), was estimated by varying the shape parameter, γ, and using two different values of separation (d) between indenters, and three different values of K_{IC} with the middle value corresponding to Douglas fir (26).

Scanning electron micrographs of the bored regions of Arabica wood shows a pattern (Fig. 10A, B) of wood damage caused by the mandibles. These data show that loads applied on the wood fibers using a specialized tool helps produce small chip sizes which are suitable for ingestion without the tool itself undergoing fracture during cutting. The energy required to puncture a substrate by a tool is a function of the tool size and the required depth of penetration. The use of sharper tools in smaller animals ensures a higher stress during substrate contact which reduces the energy required to create a puncture or a fracture [51]. The shape of the mandible edge hence seems to be optimized for optimal cutting of wood chips. Physiological responses including detoxification of defensive allele-chemicals and breakdown of secondary metabolites with resident microbes also aid the beetle in the ingestion of wood [52].
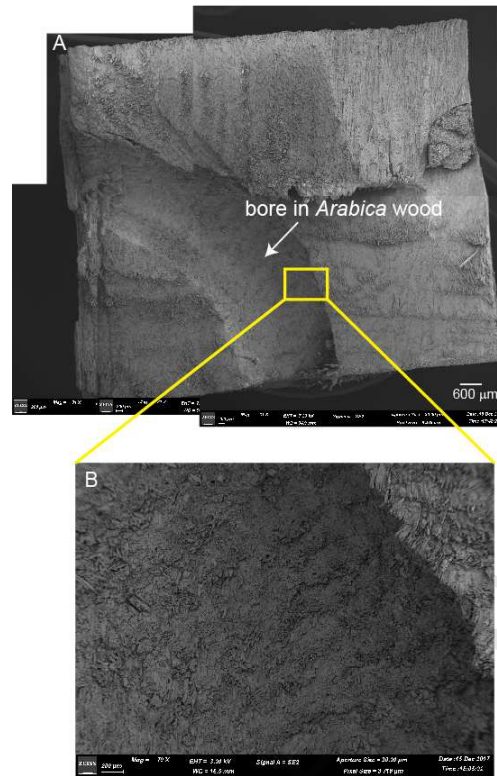
Figure 10A: SEM of the *Arabica* wood sample shows the bored region which was obtained after sectioning the sample. **B.** Enlarged bored region shows a pattern of fractured wood fibers that was caused by the sharp mandible tip.

4. Conclusions

There are several key implications of this study. First, from a biomechanics perspective, we show that the mandible functions as a highly sharp structure, akin to a knife-edge, which is used to initiate fractures in wood. We used nanoindentation experiments to show functionally graded material properties in the mandible. Peak stresses are present in the mandible tip during cutting and reduced bending stresses at the mandible base. The lower material volume due to the presence of a hollow region within the mandible does not compromise it's function during cutting. We develop a finite element model using three different boundary conditions to represent the action of the mandible during cutting. We show that the stress distributions on the

28

front and back surfaces of the mandible are significantly different. The region adjacent to the mandible tip and located away from the base of the mandible showed the maximum changes in stress values. Second, we show that the incorporation of zinc in the cutting edges increases the material hardness-and facilitates cutting through wood. Zinc enrichment in the tips of the larval mandibles alone suggests advantages during developmental to increase the material hardness. Finally, we compared the shape of the mandible to that of standard indenters and show that the tip angle in the mandible was similar to wedge tools. We developed a scaling law by modeling the indentation of the two mandibles with a plastic and porous quasi-brittle-wood substrate. We show that the larvae can produce small chip sizes suitable for ingestion through modulation of the distance between the two mandible cutting edges; chip sizes depend on the wood properties. These adaptations make the beetle a remarkably efficient and stealthy animal that eludes detection and makes it a successful pest in economically important crops like coffee. These unique design principles may also be extended into other comparative systems, such as red palm weevils in the coconut palm, Asian long head beetles in maples, etc., that face similar challenges in the cutting of woody substrates. Biomechanical studies may aid in identifying zinc chelators as herbicides to control infestation and also brings into focus mechanical principles in nature to design bioinspired tools.

References:

1. J. E. Aukema, B. Leung, K. Kovacs, C. Chivers, *et al* 2011 Economic impacts of non-native forest insects in the continental. United States. *PLoS One* **6**: 1–7. (doi:10.1371/journal.pone.0024587)

2. J. Visitpanich 1994 The biology and survival rate of the Coffee Stem Borer, *Xylotrechus quadripes Chevlorat* (Coleoptera, Cerambycidae) in northern Thailand. *Japanese J. Entomol* 62: 731–745.

3. E. A. Bernays, E. A. Jarzembowski, S. B. Malcolm 1991 Evolution of insect morphology in relation to plants. *Philos. Trans. R. Soc. B Biol. Sci.* 333: 257–264. (doi:10.1098/rstb.1991.0075)

4. R. M. Schofield, M. H. Nesson, K. A. Richardson 2002 Tooth hardness increases with zinc-content in mandibles of young adult leaf-cutter ants. *Naturwissenschaften* **89**: 579–583. (doi:10.1007/s00114-002-0381-4)

5. S. A. Wainwright 1982 *Mechanical design in organisms* (Princeton University Press).

6. J. P. Charles 2010 The regulation of expression of insect cuticle protein genes *Insect Biochem. Mol. Biol.* **40**: 205–213. (doi:https://doi.org/10.1016/j.ibmb.2009.12.005)

7. J. F. V. Vincent, U. G. K. Wegst 2004 Design and mechanical properties of insect cuticle. *Arthropod Struct. Dev.* 33: 187–199. (doi:10.1016/j.asd.2004.05.006)

8. L. Kundanati, N. Gundiah 2014 Biomechanics of substrate boring by fig wasps *J. Exp. Biol.* **217**: 1946–1954. (doi:10.1242/jeb.098228)

9. J. Hillerton, J. F.V. Vincent 1982 The specific location of zinc in insect mandibles *J. Exp. Biol.*, 333–336.

10. S. O. Andersen 2010 Insect cuticular sclerotization: A review *Insect Biochem. Mol. Biol.* 40: 166–178. (doi:10.1016/j.ibmb.2009.10.007)

11. T. L. Hopkins, K. J. Kramer 1992 Insect cuticle sclerotization *Annu. Rev. Entomol.* 37: 273–302. (doi:10.1146/annurev.en.37.010192.001421)

12. J. D. Currey 1999 The design of mineralized hard tissues for their mechanical functions *J. Exp. Biol.* 202: 3285–3294.

13. B. W. Cribb, A. Stewart, H. Huang, R. Truss, B. Noller, R. Rasch, M.P. Zaluki 2008 Unique zinc mass in mandibles separates drywood termites from other groups of termites *Naturwissenschaften*. **95**: 433–41. (doi:10.1007/s00114-007-0288-1)

14. R. M. Schofield, J. H. Postlethwait, H. W. Lefevre 1997 MeV-ion microprobe analyses of whole Drosophila suggest that zinc and copper accumulation is regulated storage not deposit excretion *J. Exp. Biol.* **200**: 3235–3243.

15. C. C. Broomell, M. A. Mattoni, F. W. Zok, J. H. Waite 2006 Critical role of zinc in hardening of *Nereis jaws* J. Exp. Biol. **209**: 3219–25. (doi:10.1242/jeb.02373)

16. C. C. Broomell, F. W. Zok, J. H. Waite 2008 Role of transition metals in sclerotization of biological tissue. *Acta Biomater.* 4: 2045–2051. (doi:10.1016/j.actbio.2008.06.017)

17. D. Quicke, P. Wyeth, J. D. Fawke, H. H. Basibuyuk, J. F. V. Vincent 1998 Manganese and zinc in the ovipositors and mandibles of hymenopterous insects *Zool. J. Linn. Soc.* 124: 387–396. (doi:10.1111/j.1096-3642.1998.tb00583.x)

18. M.G. Venkatesha, A.S. Dinesh 2012 The coffee white stemborer *Xylotrechus quadripes* (Coleoptera: Cerambycidae): bioecology, status and management. *Int. J. Trop. Insect. Sci.* **32**(4):177–188. (doi:10.1017/S1742758412000331)

19. Jansen S, Robbrecht E, Beeckman H, Smets E. 1997 Comparative wood anatomy of African Coffeeae (Rubiaceae-Ixoroideae). *Belgian J. Bot.* **130**.

20. Chave, Jerome. 2005 "Measuring wood density for tropical forest trees. A field manual for the CTFS sites", Lab. Evolution et Diversite' Biologique, Universite' Paul Sabatier, 31000 Toulouse, France. 1-7.

21. B. D. Metscher 2009 MicroCT for comparative morphology: simple staining methods allow high-contrast 3D imaging of diverse non-mineralized animal tissues *BMC Physiol.* **9**: 11. (doi:10.1186/1472-6793-9-11)

22. B. J. Briscoe, L. Fiori, E. Pelillo 1998 Nano-indentation of polymeric surfaces *J. Phys. D. Appl. Phys.* 31: 2395–2405.

23. W. C. Oliver, G. M. Pharr 2004 Measurement of hardness and elastic modulus by instrumented indentation: Advances in understanding and refinements to methodology *J. Mater. Res.* **19**: 3–20. (doi:10.1557/jmr.2004.19.1.3)

24. S. Combes, T. L. Daniel 2003 Flexural stiffness in insect wings I. Scaling and the influence of wing venation. *J. Exp. Biol.* 206, 2979–2987.

31

25. A. Khalife, R. A. Keller, J. Billen, F. H. Garcia, E. P. Economo, C. Peeters 2018 Skeletomuscular adaptations of head and legs of *Melissotarsus* ants for tunneling through living wood *Frontiers Zoo.* doi: 10.1186/s12983-018-0277-6.

26. J. Goyens, J. Dirckx, M. Dierick, L. van Hoorebeke, P. Aerts 2014 Biomechanical determinants of bite force dimorphism in *Cyclommatus metallifer* stag beetles *J. Exp. Biol.* **217:** 1065-71.

27. D. E. Kretschmann, 2010 Chapter 5 - Mechanical Properties of Wood. *Wood Handbook - Wood as an Engineering Material*, General Technical Report FPL–GTR–190, United States department of Agriculture 1–46.

28. B. Lawn, R.Wilshaw 1975 Indentation Fracture: Fracture and Applications. *J. Mater . Sci.* **10**, 1049–81.

29. A. Evans., E.Charles 1976 Fracture Toughness Determination by Indentation. *J. Am. Ceram. Soc.* , 371–372

30. G. R. Anstis, P. Chantikul, B. R. Lawn, D. B. Marshall 1981 A critical evaluation of indentation techniques for measuring fracture toughness: I, Direct Crack Measurements. *J. Am. Ceram. Soc.* **46**, 533–538.

31. D. K. Shetty, A. R. Rosenfield, W. Duckworth 1985 Analysis of indentation crack as a wedge-loaded half penny crack. *J. Am. Ceram. Soc.* **61**, 65–67.

32. R. S. Ruoff, N. M. Pugno 2004 Quantized fracture mechanics. *Philos. Mag.* **84**, 2829–2845. (doi:10.1080/14786430412331280382)

33. N. M. Pugno 2007 The role of defects in the design of space elevator cable: From nanotube to megatube. *Acta Mater.* **55**, 5269–5279. (doi:10.1016/j.actamat.2007.05.052)

34. M. Vincent, Q. Tong, N. Terziev, G. Daniel, C. Bustos, W. G. Escobar, I. Duchesne 2014 A comparison of nanoindentation cell wall hardness and Brinell wood hardness in jack pine (Pinus banksiana Lamb.). *Wood Sci. Technol.* **48**, 7–22. (doi:10.1007/s00226-013-0580-5)

35. B.W. Cribb, et al. 2008 Unique zinc mass in mandibles separates drywood termites from other groups of termites. *Naturwissenschaften* **95** (5):433–41.(doi: 10.1007/s00114-008-0346-3)

36. H. Ming-Yuan, J. W. Hutchinson 1989 Crack deflection at an interface between dissimilar elastic materials *Int. J. Solids Struct.* 25: 1053–1067.

32

37. Bar-On B, Barth FG, Fratzl P, Politi Y 2014 Multiscale structural gradients enhance the biomechanical functionality of the spider fang. *Nat. Commun.* 5:3894. (doi:10.1038/ncomms4894)

38. Y. Politi, B. Bar-On, H. O. Fabritius 2019 *Mechanics of arthropod cuticle-versatility by structural and compositional variation. In architectured materials in Nature and engineering* (pp. 287-327). Springer, Cham.

39. B. Bar-On 2019 On the form and bio-mechanics of venom-injection elements. *Acta Biomaterialia* 85, 263-271.

40. A. van der Meijden, T. Kleinteich, P. Coelho 2012 Packing a pinch: Functional implications of chela shapes in scorpions using finite element analysis *J. Anat.* 220: 423–434. (doi:10.1111/j.1469-7580.2012.01485.x)

41. S. Timoshenko 1940 *Strength of materials* (D. Van Nostrand Company, Incorporated)

42. F. J. Clissold 2007 The biomechanics of chewing and plant fracture: Mechanisms and implications *Adv. In Insect Phys.* **34**: 317–372. (doi:10.1186/1741-7007-5-6)

43. S. E. Stanzl-tschegg 2006 Microstructure and fracture mechanical response of wood *Int. J. Fracture* **139**: 495–508. (doi:10.1007/s10704-006-0052-0)

44. S. E. Stanzl-tschegg, P. Navi 2009 Fracture behaviour of wood and its composites. A review COST Action E35 2004 – 2008 : Wood machining – micromechanics and fracture. 63, 139–149. (doi:10.1515/HF.2009.012)

45. E. Wilson, M. S. Mohammadi, J. A. Nairn 2015 Crack propagation fracture toughness of several wood species. (doi:10.1520/ACEM20120045)

46. M.P.C. Conrad, G.D. Smith 2003 Fracture of solid wood: A review of structure and properties at different length scales. *Wood Fibre Sci.* 35, 57–584.

47. A. Saoud, A. Elamri, K. Kimakh, M. Chergui 2018 Mechanical behavior of wood subjected to mode II fracture , using an energetic criterion: Application on THUJA of Morocco. **44**, 25–34. (doi:10.3221/IGF-ESIS.44.03)

48. L. Gibson, M. Ashby 1997 Wood. In *Cellular Solids: Structure and Properties* (Cambridge Solid State Science Series, pp. 387-428). Cambridge: Cambridge University Press. doi:10.1017/CBO9781139878326.012

49. R. Hock 2009 *The perfect edge : The Ultimate guide to sharpening for wood-workers* Popular wood working books. (doi:10.1007/s11340-007-9051-y)

33

50. K. Muhammad Usman 2012 Effects of tool rake angle on tool life in turning tools. *Int J Sci Eng Res* 3(4):1–6.

51. P. S. Anderson 2018 Making a point: shared mechanics underlying the diversity of biological puncture. *J. Exp. Biol.* 221(22), jeb187294.

52. K.M. Oliver, A.J. Martinez 2014 How resident microbes modulate ecologically-important traits of insects. *Curr. Opin. Insect. Sci.* 4(1):1–7.(doi:10.1016/j.cois.2014.08.001)

Sample	Stiffness (N/mm)			Hardness (GPa)		
	Region1	**Region2**	**Region3**	**Region1**	**Region2**	**Region3**
1	5.56±1.06	10.82±3.04	7.63±1.09	0.40±0.01	0.51±0.18	0.52±0.17
2	11.27±3.12	8.77±0.55	7.00±0.47	0.29±0.06	0.39±0.09	0.88±0.31
3	11.26±1.2	5.68±0.11	6.73±0.29	0.33±0.04	0.30±0.01	0.50±0.08
4	9.73±1.98	10.26±0.49	7.31±0.74	0.38±0.05	0.36±0.04	0.51±0.13
5	10.92±1.45	10.06±0.16	6.63±0.19	0.34±0.03	0.41±0.01	0.52±0.14
6	9.85±3.10	8.82±0.34	5.60±0.34	0.29±0.03	0.43±0.01	0.68±0.10
7	8.35±1.72	7.13±0.14	6.67±0.28	0.33±0.04	0.39±0.02	0.69±0.11
8	8.01±0.80	8.77±0.07	8.09±1.03	0.49±0.10	0.46±0.20	1.08±0.28
9	7.32±0.64	7.37±1.71	8.50±0.91	0.39±0.05	0.36±0.09	0.61±0.12
Average	**9.14±1.97**	**8.63±1.66**	**7.13±0.87**	**0.36±0.06**	**0.40±0.06**	**0.67±0.20**

Table A1: Stiffness and hardness from the three different mandible regions, marked in Fig. 5D, were calculated by analyzing the force-depth curves using nanoindentation results at each location (n=9) on a given specimen. Data are reported as average ± stdev for each sample; the last row in the table shows the overall average for each of the three regions.

d (μm)	γ	$\delta_{el\text{-}pl}$ (μm)	δ_{el} (μm)	$\delta_{hy\text{-}el}$ (μm)	d (μm)	γ	$\delta_{el\text{-}pl}$ (μm)	δ_{el} (μm)	$\delta_{hy\text{-}el}$ (μm)
	0.01	445	445	445		0.01	441	440	439
	0.1	489	488	478		0.1	445	443	441
	0.5	744	740	735		0.5	466	454	443
	0.8	1020	1010	1001		0.8	483	463	445
500	1	1259	1244	1229	100	1	494	469	446
	1.2	1553	1531	1510		1.2	505	476	447
	1.4	1917	1885	1854		1.4	517	482	449
	1.5	2129	2091	2054		1.5	523	485	449
	2	3601	3517	3434		2	554	501	453

Table A2: Depth of cut value ($\delta_{el\text{-}pl,}$ $\delta_{el,}$ δ_{el}) was estimated by varying the shape parameter, γ, and using two different values of separation between indenters, d, with K_{Ic} = 0.4 MPa$\sqrt{\text{m}}$ corresponding to Douglas fir (26).

D (μm)	γ	$\delta_{el\text{-}pl}$ (μm)	δ_{el} (μm)	$\delta_{hy\text{-}el}$ (μm)	d (μm)	γ	$\delta_{el\text{-}pl}$ (μm)	δ_{el} (μm)	$\delta_{hy\text{-}el}$ (μm)
K_{IC} = 0.04 MPa$\sqrt{\text{m}}$					K_{IC} = 4 MPa$\sqrt{\text{m}}$				
	0.1	397	395	393		0.1	499	497	494
100	0.5	262	256	249	100	0.5	829	808	788
	1	156	148	141		1	1313	1248	1187
	0.1	435	435	435		0.1	539	538	538
500	0.5	418	416	413	500	0.5	1214	1206	1199
	1	398	393	389		1	3347	3308	3269

Table A3. Depth of cut, ($\delta_{el\text{-}pl,}$ $\delta_{el,}$ δ_{el})**,** was estimated by varying K_{Ic} for two different cases with variations in the bite distance, d. δ varies directly with K_{Ic} under conditions for the cracks to meet